Direct numerical simulation of turbulent flow over a backward-facing step

Michal A. Kopera[1]†, Robert M. Kerr[2]‡ Hugh M. Blackburn[3] and Dwight Barkley[2]

[1] Department of Applied Mathematics, Naval Postgraduate School, Monterey, CA, 93940

[2] Mathematics Institute, University of Warwick, Coventry CV4 7AL, United Kingdom

[3] Department of Mechanical and Aerospace Engineering, Monash University, 3800 Australia

(Received 21 October 2014)

Turbulent flow in a channel with a sudden expansion is simulated using the incompressible Navier-Stokes equations. The objective is to provide statistical data on the dynamical properties of flow over a backward-facing step that could be used to improve turbulence modeling. The expansion ratio is $E_R = 2.0$ and the Reynolds number, based on the step height and mean inlet velocity, is $Re_h = 9000$. The discretisation is performed using a spanwise periodic spectral/hp element method. The inlet flow has turbulent velocity and pressure fields that are formed by a regenerating channel segment upstream of the inlet. Time and spanwise averages show secondary and tertiary corner eddies in addition to the primary recirculation bubble, while streamlines show a small eddy forming at the downstream tip of the secondary corner eddy. This eddy has the same circulation direction as the secondary vortex. Analysis of three-dimensional time-averages shows a wavy spanwise structure that leads to spanwise variations of the mean reattachment location. The visualisation of spanwise averaged pressure fluctuations and streamwise velocity shows that the interaction of vortices with the recirculation bubble is responsible for the flapping of the reattachment position, which has a characteristic frequency of $St = 0.078$.

1. Introduction

1.1. *Motivation*

The flow over a backward-facing step (BFS) is a prototype for separating, recirculating and reattaching flow in nature and in numerous engineering applications. Examples include the flows around buildings, inside combustors, industrial ducts and in the cooling of electronic devices. In all these cases the presence of separation, recirculation and reattachment drastically changes the transport of momentum and heat within the flow. In aeronautical separation this results in a loss of the lift force and increased drag and inside an expanding duct recirculation influences the recovery of the flow downstream from the expansion. In combustors, the presence of a shear layer between the main flow and the recirculation bubble can increase the mixing of fuel and oxidiser and in electronic systems the recirculation zone changes the cooling properties of the flow. All of those examples share one common feature: That an adverse pressure gradient (usually due to a sudden change of geometry) causes the boundary layer to separate from the surface and form a mixing layer, which eventually reattaches to the surface. The backward-facing step is a

† Email address for correspondence: makopera@nps.edu
‡ Email address for correspondence: rmkerr@warwick.ac.uk

prototype of these scenarios, as it demonstrates the phenomena with a simple geometry, one that is easy to set-up experimentally, as well as model computationally.

In addition, the geometry of the BFS is the next most complicated paradigm for the direct numerical simulation (DNS), after the flows exhibiting periodicity in the streamwise direction - like the channel or pipe flow. To the Authors' knowledge, there has been only one publication regarding three-dimensional DNS of turbulent flow over a BFS by Le *et al.* (1997).

The primary goals are to provide the turbulence modelling community with the types of the statistics and instantaneous flow field data that are needed for improving the models for separation, recirculation and reattachment in turbulent flows, as well as provide new insight into the structure and dynamics of the flow.

1.2. *Survey of previous work*

BFS flow has been investigated experimentally many times. Early work with expansions on one or both walls is reviewed by Abbot & Kline (1962) and an extensive overview of experiments on recirculating flows in different configurations performed up to 1970, plus their own work, is provided by Bradshaw & Wong (1972). Since then there have been a number of experimental studies that examined similar configurations with expansions (Kim *et al.* 1980; Durst & Tropea 1981; Armaly *et al.* 1983; Adams & Johnston 1988; Jovic & Driver 1995; Spazzini *et al.* 2001). The experiments most relevant to the current work are Yoshioka *et al.* (2001) and Hall *et al.* (2003).

The first two-dimensional simulations addressed only the mean flow over a BFS, either laminar (Armaly *et al.* 1983) or a transitional study with $Re_0 = UH/\nu = 1.65 \times 10^5$, based on the step height H and centreline inlet velocity U (Friedrich & Arnal 1990). Coherent structures within a BFS were first identified in both two- and three-dimensions by using a prescribed inlet velocity profile and superimposed noise applied to direct and large-eddy simulations (Silveira Neto *et al.* 1993).

True comparisons with experimental statistics began with the Le *et al.* (1997) simulations of a BFS in an open channel. They used an expansion ratio of $E_R = 1.2$ at $Re = UH/\nu = 5100$ to obtain a characteristic frequency of reattachment of $St = 0.06$, a mean reattachment length of $X_r = 6.28$, and the instantaneous reattachment location varied in the spanwise direction, all in agreement with a concurrent experimental study (Jovic & Driver 1994). In the recirculation zone a very high negative skin friction coefficient was found, which was attributed to a relatively low Reynolds number, and the velocity profiles at long distances downstream were not fully developed, which was consistent with slow regeneration of the velocity profile after reattachment.

Le *et al.* (1997) became a reference for all turbulence models and set a standard in separated turbulent flow simulations by providing the budgets of all Reynolds stress components and reporting averaged velocity and pressure fields. This paper documents many similarities between the properties of the two simulations, Le *et al.* (1997) and here, despite differences in the Reynolds numbers, nature of the inflow and whether it is an open or closed channel. Then extends their DNS database of turbulent backward-facing flows to higher Reynolds numbers, as well as providing an in-depth analysis of the fluctuations underlying the oscillations of the reattachment line in terms of velocities, vortex structures, wall shear stresses and frequency spectra. The goal is to provide us with a more complete picture of the origins of the reattachment oscillations, a picture that can then be applied to other flows with oscillatory behaviour.

This paper is organized as follows: Section 2 presents the governing equations, boundary conditions and numerical methods used for the simulations. Section 3 provides a discussion of the results, including the inlet velocity profiles, reattachment length, aver-

aged and instantaneous velocity and pressure fields. The data is validated by comparison with existing experimental and numerical results. The analysis of average flow fields provides an insight into the structure of the flow and is followed by the investigation of dynamic behavior of the reattachment position. The paper is concluded in Section 4.

2. Equations, approximations and scaling

2.1. *Governing equations*

The flow over a backward-facing step is governed by the incompressible Navier-Stokes momentum equation

$$\frac{\partial \boldsymbol{u}}{\partial t} + (\boldsymbol{u} \cdot \nabla)\boldsymbol{u} = -\frac{1}{\rho}\nabla p + \nu \Delta \boldsymbol{u} \tag{2.1}$$

with the continuity constraint

$$\nabla \cdot \boldsymbol{u} = 0, \tag{2.2}$$

where $\boldsymbol{u} = \{u_i\} = [u, v, w]$ is the velocity vector, ρ is a constant density, p is pressure and ν is kinematic viscosity. Eq. (2.1) can be rewritten as

$$\frac{\partial u_i}{\partial t} = -\frac{\partial p}{\partial x_i} - \nu \Delta u_i + \mathbb{N}_i(\boldsymbol{x}), \tag{2.3}$$

where the nonlinear term

$$\mathbb{N}_i(\boldsymbol{x}) = -u_j \frac{\partial u_i}{\partial x_j}. \tag{2.4}$$

In all the above equations the summation convention applies.

2.2. *Geometry and boundary conditions*

The primary case simulated here consists of a flow inside a channel with a one-sided sudden expansion, with figure 1 giving an overview of the geometry along with a schematic of the inlet and outlet boundary conditions. The coordinate frame is defined by (x, y, z) axis, where x indicates the streamwise, y the vertical and z the spanwise directions and the origin of the coordinate frame is located at the bottom of the step at the rear end of the span of the domain.

The inlet channel is $L_i = 12h$ long with its height equal to h and the outlet channel has dimensions $L_x = 29h$ and $L_y = 2h$, giving an expansion ratio of $E_R = \dfrac{L_y}{L_y - h} = 2$. The computational domain Ω is defined as:

$$\Omega : (x, y, z) \in [-12h, 0] \times [h, 2h] \times [0, 2\pi h] \quad \cup \quad [0, 29h] \times [0, 2h] \times [0, 2\pi h]. \tag{2.5}$$

The walls confining the channel are modelled as no-slip walls with Dirichlet boundary conditions of $\boldsymbol{u} = 0$. The wall at $y = 2h$ (further referred to as the top wall) is defined as:

$$\partial\Omega_t : (x, y, z) \in [-12h, 29h] \times \{2h\} \times [0, L_z] \tag{2.6}$$

and the step wall (also referred to as the bottom wall) is defined as:

$$\begin{aligned} \partial\Omega_b : (x, y, z) \in & [-12h, 0] \times \{h\} \times [0, L_z] \\ & \cup \{0\} \times (0, h) \times [0, L_z] \\ & \cup [0, 29h] \times \{0\} \times [0, L_z]. \end{aligned} \tag{2.7}$$

The channel is periodic in the spanwise direction with a periodic length of $L_z = 2\pi h$. The periodic length was chosen based on results by Le (1995, $L_z = 4.0h$), Schafer *et al.* (2009,

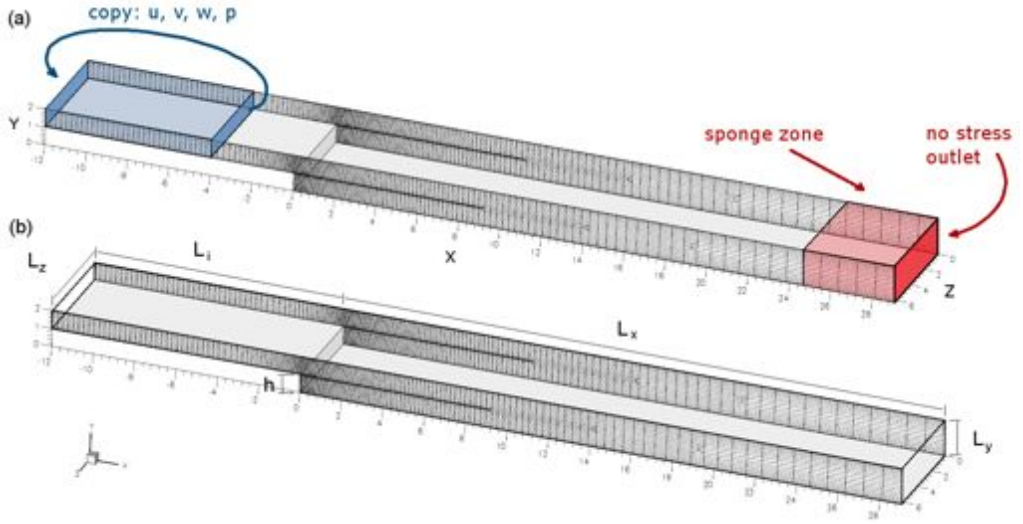

FIGURE 1. **Geometry overview** - (a) schematics of inlet and outlet boundary conditions, (b) dimensions of the domain

$L_z = \pi h$) and Kaikstis *et al.* (1991, $L_z = 2\pi h$). Le (1995) reports that a periodic length of $L_z = 4.0h$ was adequate to tail off the two-point correlations for u, v and w near the wall, however away from the wall in the free shear layer some correlations remained at approximately 10%. One reason is the presence of spanwise rollers in the free shear layer, which the present study addresses by making the periodic dimension over 50% wider to be certain that all spanwise structures are well represented.

To ensure that the flow was fully turbulent by the time of the step, the boundary condition at the inlet to the domain followed the example of Lund *et al.* (1998). The method extracts a vertical plane of velocity and pressure data from an auxiliary simulation of a periodic, regenerating wall bounded flow and uses this place to define a time-dependent Dirichlet boundary condition at the inlet plane. In the present study the regeneration zone is placed upstream of the step. This is schematically presented in figure 1 (a). The length of the regeneration section is $L_r = 8h$ and the boundary condition it generates will be referred to as the *copy* boundary condition. The validation of this technique is presented in Section 3.1. Details of the implementation to Semtex can be found in Cantwell (2009).

$$\begin{aligned} \boldsymbol{u}\,|_{\partial\Omega_i} = \boldsymbol{u}\,|_{\partial\Omega_r} \qquad & \partial\Omega_i : (x,y,z) \in \{-12h\} \times [h,2h] \times [0,2\pi h] \\ & \partial\Omega_r : (x,y,z) \in \{-12h + L_r\} \times [h,2h] \times [0,2\pi h]. \end{aligned} \tag{2.8}$$

A conventional outlet boundary condition is prescribed at $\partial\Omega_o$ as follows:

$$\nabla\boldsymbol{u}\cdot\boldsymbol{n}\,|_{\partial\Omega_o} = 0 \quad \partial\Omega_o : (x,y,z) \in \{29h\} \times [0,2h] \times [0,2\pi h], \tag{2.9}$$

where $\boldsymbol{n}$ is a unit vector perpendicular to $\partial\Omega_o$. Due to the concerns that the Neumann condition might not advect the flow structures out of the domain properly, an optional sponge zone was implemented in the area $2h$ upstream of the outflow in order to dampen excessive oscillations. The sponge zone was implemented by adding this forcing term to Eq. (2.1):

$$\boldsymbol{F_s} = -\alpha_s(\boldsymbol{u} - \boldsymbol{U_s}), \tag{2.10}$$

where $\boldsymbol{U_s}$ is a prescribed velocity profile obtained and rescaled from the inlet channel,

and α_s is a parameter regulating the forcing amplitude. The aim of the sponge zone was to force the turbulent flow towards the prescribed profile. In the course of preliminary simulations it turned out that the length of the outflow channel was sufficient for the flow to regenerate enough to be advected by the Neumann condition (2.9) without additional forcing, therefore in the main simulation $\alpha_s = 0$.

2.3. *Space discretization and numerics*

The flow defined in Sec. 2.1 and 2.2 was simulated using a spectral element method code Semtex (Blackburn & Sherwin 2004), which discretizes the solution in x and z using a two-dimensional spectral/hp element method (SEM), and Fourier transform in y. The numerical code uses the stiffly-stable multi-step velocity-correction method of Karniadakis *et al.* (1991), including the pressure sub-step that imposes the appropriate boundary conditions (Orszag *et al.* 1986).

The 2D SEM used in this work consists of the expansion of the solution in the polynomial base on quadrilateral elements which pave the entire computational domain. The element mesh is block-structured with non-structured elements near $(x, y) = (9h, h)$, $(x, y) = (14h, h)$ and $(x, y) = (19h, h)$. The non-structured elements were introduced in order to coarsen the vertical resolution in the middle part of the channel and maintain at the same time the conformity of the grid, which is a requirement for the software used for the simulation.

The mesh in the inlet channel consists of 11 elements in the vertical direction. Each element consists of 11 nodal points in each direction, which gives a total of 121 nodal points in the vertical direction. Only 111 of them are unique, because nodal points at elemental boundaries coincide and the C^0 continuity is enforced across the boundary. The distribution of element vertexes, which define the elements, mimic the Chebyshev distribution, following a good practise guidelines for SEM DNS of channels (Karniadakis & Sherwin 2005, p.475). The size of the element closest to the wall is approximately 16 wall units, based on the friction velocity measured at $x = -8h$ in the inlet channel. With 11 nodal points inside an element, the first point away from the wall is located at $\Delta y^+ = 0.528$.

In the streamwise direction the mesh is uniform in the periodic (regeneration) part of the inlet channel, with the element size $\Delta x = 0.25h$ which corresponds to $\Delta x^+ \approx 136$ for an element, and Δx^+ between 4.5 and 20.1 for nodal points within each element. It is gradually refined from $x = -4h$ to $x = 0$, and it slowly coarsens downstream of the step. The smallest streamwise element size near the step has $\Delta x^+ \approx 27$, which corresponds to the smallest distance between the nodes of $\Delta x^+ \approx 1.78$. A single $x - y$ slice of the domain consists of 2845 2D elements and 344245 nodal points. The structure of the mesh in the entire domain is depicted in Fig. 1.

The number of collocation points in the spanwise direction $N_z = 128$, which corresponds to 64 Fourier modes, is doubled as compared to Le (1995), which results in higher resolution as the spanwise domain size is only increased by over 50%. This is to avoid problems with resolving small-scale structures at $y^+ < 10$, as reported by Le (1995).

2.4. *Simulation parameters*

The maximum Reynolds number, given the limitations of the code and resources, was derived using the usual estimate for the number of points N needed to resolve all scales in a turbulent flow: $N \sim Re^{9/4} = (Re^{3/4})^3$ on a uniform grid, where $Re^{3/4}$ is the ratio of the largest length scale to the Kolmogorov dissipation scale. This of course can only be an estimate for a spectral/hp element method because the number of actual colocation points is complicated function of the number of elements, their dimensions

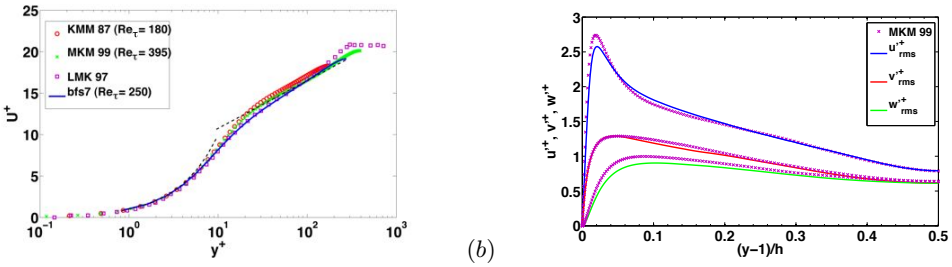

(a) (b)

FIGURE 2. (a) Inlet velocity mean U and (b) fluctuations $u'_{rms}, v'_{rms}, w'_{rms}$ profiles time and spanwise averaged at $x = -2.0$. The statistics were collected over an averaging time of $T_{ave} \approx 200h/U_b$ with a sampling frequency $f_{ave} = 40U_b/h$. Profiles are compared with results of turbulent channel flow DNS simulations of Kim *et al.* (1987, denoted as KMM87), Moser *et al.* (1999, denoted as MKM99) as well as the backward-facing step simulation of Le *et al.* (1997, denoted as LMK97). bfs7 denotes current simulation.

which depend upon their location with respect to the boundaries, and the number of spectral functions/element. For the primary calculation in the paper 2845 2D element mesh on the HECToR XT4 system were used. The solution within each 2D element was expanded using 10^{th} order polynomials on 121 collocation points, which gave 344245 nodal points per 2D mesh. In the spanwise direction we used $N_Z = 128$ equispaced points, which brought the total number of points in the domain to $\approx 4.4e^7$. The mesh of this size allowed for running a $Re_h = 9000$ simulation with the time step of $dt = 0.5e^{-3}$.

3. Results

To validate the main simulation, the following characteristics were compared with the data from simulations and experiments. The velocity profile of the copy inflow condition was compared with the results of other turbulent channel flow simulations. For the BFS flow, the reattachment length was determined by averaging the coefficient of friction along the bottom wall and compared with previous work. In order to confirm that the streamwise and vertical resolution is adequate, the grid spacing was compared with the Kolmogorov scale. Finally, the spanwise modal energy decay in the shear layer was used to determine whether the N_Z resolution was adequate.

3.1. *Inlet*

Figure 2(a) shows the U velocity profile in the inlet section of the domain. The results collapse reasonably well with the current simulation showing the same slope in the log layer as in Le *et al.* (1997), which is slightly different from the channel flow profiles (Kim *et al.* 1987; Moser *et al.* 1999). In absence of the present simulation data, one could conclude that the difference is due to turbulent inflow condition in the BFS simulation. The agreement between Le *et al.* (1997) and current simulation, even though turbulent inflow conditions are different, suggests that the step is responsible for the difference in the velocity profile slopes in the boundary layer.

Figure 2(b) compares the turbulence intensity profiles with a turbulent channel flow simulation (Moser *et al.* 1999) and finds good qualitative agreement between all three profiles and the reference data. There are some noticeable differences, particularly in the peak of u'_{rms} and w'_{rms} profiles. Again, this difference might be attributed to the presence of the step in the current (bfs7) simulation.

Apart from the statistical properties of the flow in the inlet section, another concern was the influence of the length of the inlet channel and the role of the periodic (inlet

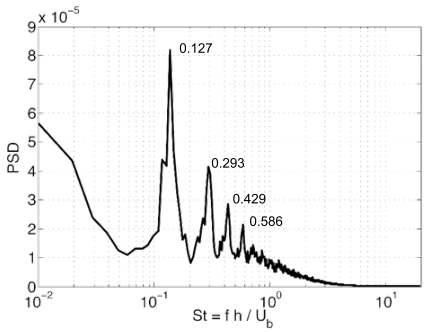

FIGURE 3. **Power spectrum of** u' - power spectral density of spanwise averaged u' velocity fluctuation at $x = -2.0, y = 1.5$. The periodic regeneration area introduces an artificial frequency $St = 0.127$, and its harmonics, which corresponds to the periodic area length of $8h$.

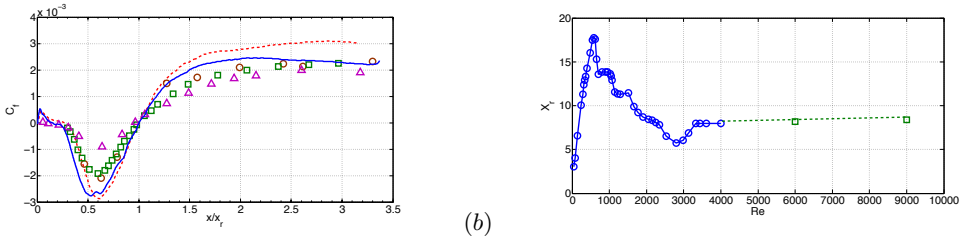

(*a*) (*b*)

FIGURE 4. (a) Coefficient of friction and (b) reattachment length X_r compared with experimental and simulation results. Our coefficient of friction (blue solid line) is compared with results of turbulent channel flow DNS simulations of Le *et al.* (1997)(dashed red line) and experiments by Adams & Johnston (1988)(triangles), Jovic & Driver (1995) (circles) and Spazzini *et al.* (2001). The reattachment length is compared with Armaly *et al.* (1983) (circles).

regeneration) section on the dynamics of the flow. The power spectrum of Fig. 3 shows that the periodic regeneration area introduces an artificial frequency $St = 0.127$, and its harmonics, which corresponds to the periodic area length of $8h$. This could have been avoided by increasing the periodic area length, and increasing the computational cost of the simulation. Therefore the periodic length was kept at $8h$ to regenerate the turbulent properties of the flow after they break down at the inlet, similar to the $7h$ length used by Le (1995). A thorough examination of spectra at different locations in the flow, which shows that the recycling frequency does not have any significant influence on the dynamics of the flow, is presented in Section 3.10.2.

3.2. *Reattachment length and coefficient of friction*

The *reattachment length* (X_r) is defined as the average distance from the step edge to the flow reattachment position, which can be determined from the zeros of the coefficient of friction (C_f) at the bottom wall. Figure 4a compares our coefficient of friction with the computational data (Le *et al.* 1997) and the experiments (Adams & Johnston 1988; Jovic & Driver 1995; Spazzini *et al.* 2001), with the comparison data coming from cases without a top wall. Cases with $E_R = 2.0$ are not included because they either do not report C_f or deal with laminar or transitional flow.

Because the comparison cases use the maximum inlet velocity U_0 to scale C_f, whereas we are using the mean bulk velocity at the inlet U_b to set velocity scales, for C_f we will use $U_0 = 1.22U_b$.

The relative proximity of the minima of the coefficients of friction between the current

Case	Re_h	X_r	E_R	$C_{f,min}$	$X_{(C_{f,min})}/X_r$
bfs7	9000	8.62	2.0	$-2.9 \cdot 10^{-3}$	0.62
bfs6	6000	8.16	2.0	$-3.12 \cdot 10^{-3}$	0.53
Le *et al.* (1997)	5100 (4250*)	6.28	1.2	$-2.89 \cdot 10^{-3}$	0.61
Armaly *et al.* (1983)	8000 (4000*)	8.0	2.0	-	-
Adams & Johnston (1988)	36000 (30000*)	6.3	1.25	$-0.885 \cdot 10^{-3}$	0.63
Jovic & Driver (1995)	10400 (8700*)	5.35	1.09	$-2.0 \cdot 10^{-3}$	0.63
Spazzini *et al.* (2001)	10000 (8300*)	5.39	1.25	$-1.87 \cdot 10^{-3}$	0.6
Chandrsuda & Bradshaw (1981)	10^5	6.0	1.4	-	-

TABLE 1. Reattachment length and coefficient of friction. The values of Re with * are scaled using U_b.

case and Le *et al.* (1997) were a surprise. Owing to the roughly doubled Reynolds number one would have expected the minima of C_f to decrease. Instead, the minimal peak is slightly shifted upstream. One reason for this might be that we are comparing two different cases, one with the top wall and one without. Also, the discrepancy between Le *et al.* (1997) and other results in the regeneration zone could be due to low Reynolds number effects, as this case has relatively low Re_h.

Table 1 shows X_r values for a number of computational and experimental studies, along with the peak negative C_f, its position downstream from the step, the expansion ratio E_R and Reynolds number for each case. Cases bfs6 and bfs7 represent the simulations performed in the frame of this study. Since different authors use different scaling quantities, in brackets we provide Re scaled using bulk mean velocity and step height to be able to compare directly with our data.

Armaly *et al.* (1983), which used the same expansion ratio as the present study, showed that X_r depends strongly on Re in the laminar and transitional regime, but with no Reynolds number dependence in the turbulent regime. Figure 4b compares their results with two reattachment lengths computed for different Reynolds number. Present results indicate that there might be a weak Re dependence of X_r in the turbulent regime, which would not have been apparent in the Armaly *et al.* (1983) study, as it only examined a few very low turbulent Re cases (up to $Re_h = 4000$, where $Re_h = 3300$ was identified as the lower limit of the turbulent regime). Similar conclusions come from the comparison of results of Spazzini *et al.* (2001) and Adams & Johnston (1988), where tripled Re causes $\approx 17\%$ increase in the reattachment length.

3.3. *Grid resolution study*

To show that the choice of grid resolution resolved the flow for a given Re_h the spectral element mesh size was compared with the Kolmogorov scale of the flow. Similar analysis was performed by Kim *et al.* (1987) for channel flow. We also looked at the modal energy decay in different points of the flow to confirm that the grid resolution in the spanwise direction was adequate.

For the purpose of this study, we define the the grid spacing to be the average distance between nodal point within the element. In other words, each element has only one value

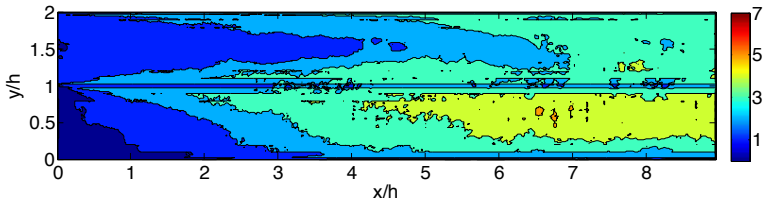

FIGURE 5. Spanwise averaged grid spacing Δ_e divided by the Kolmogorov scale η_K. The ratio does not exceed 7 in the worst case, and is below 5 in the most active regions (reattachment zone and mixing layer).

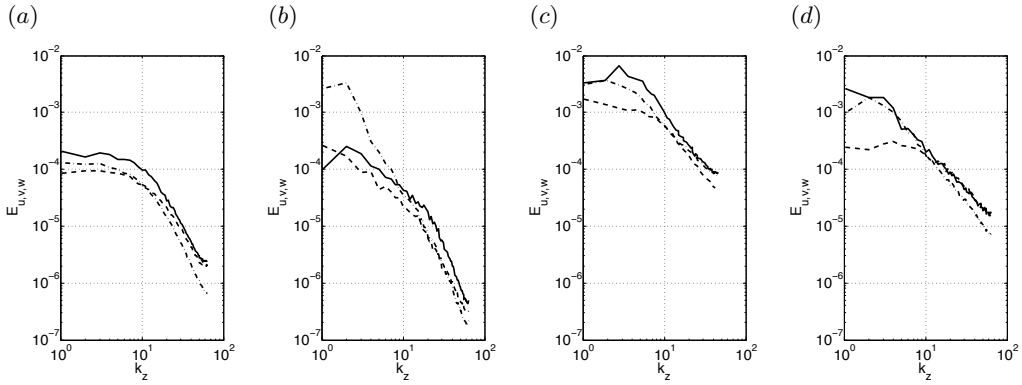

FIGURE 6. Time averaged spectrum of u' (solid line), v' (dashed line) and w' (dot-dashed line) energy at (a) $x = -2h$, $y = 1.5h$, (b) $x = 0.1h$, $y = 1h$, (c) $x = 4h$, $y = 1h$, (d) $x = 4h$, $y = 0.01h$.

of grid spacing defined within its boundaries. This spacing is defined as the size of the element divided by the number of points: $\Delta_e = (\Delta x_e \cdot \Delta y_e)^{\frac{1}{2}}/N_P$, where Δx_e and Δy_e are the streamwise and vertical sizes of the element for which the spacing is defined.

Fig. 5 presents the results of this analysis. The grid spacing was divided by the Kolmogorov scale estimated by

$$\eta_K = \left(\frac{\nu^3}{\epsilon}\right)^{\frac{1}{4}}, \tag{3.1}$$

where $\epsilon = 2\nu S_{ij} S_{ij}$ is the energy dissipation rate and S_{ij} represents the rate-of-strain tensor. For simplicity, let $r_r = \Delta_e/\eta_K$ be called the resolution ratio, plotted in Fig. 5 with the peak r_r not exceeding 7 and most of the domain satisfying $r_r < 5$. The wall regions are very well resolved with the resolution ratio below 3. This analysis shows that $\Delta = O(\eta_K)$, which confirms that the grid refinement in the x-y planes is sufficient for $Re_h = 9000$.

In order to verify the resolution in the spanwise direction, the modal energy decay in several places in the flow was examined. Fig. 6 (a) shows the result obtained in the inlet channel and figures 6 (b - d) present the results for different places in the shear layer. For all of the components at the $x - y$ positions, except for E_{vv} in 6d, as discussed in section 3.7, there are clear drops in the modal energy over at least two decades, indicating that there is adequate spanwise resolution in the shear layer.

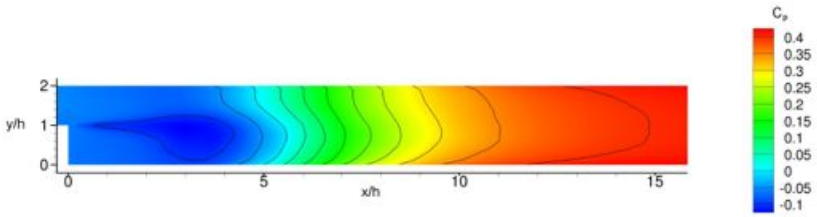

FIGURE 7. Mean static pressure coefficient contours. $C_P = \frac{P-P_0}{\frac{1}{2}\rho U_b^2}$

3.4. *Averaged flow field*

This section contains statistical data collected over the total averaging time $T_{ave} = 200h/U_b$ using 8000 samples. The averaging was initiated after an initial burn-in time of $T_{BI} = 50h/U_b$, enough for the initial transients to decay after the change of Re_h from 6000 in the preliminary simulation to 9000. T_{BI} is equal to roughly two flow-through times. The flow-through time is defined as the integral of $\dfrac{1}{U}$ along the streamline S calculated on an averaged velocity field, originating at $x = 0.0$, $y = 1.5$ and finishing at the plane $x = 20.0$.

$$T_{FT} = \int_S \frac{\mathrm{d}S}{U}.$$

The initial condition for the burn-in process was taken from preliminary simulations with $Re = 6000$ and $N_P = 11$. The length of the burn-in process selected was based on the streamwise component of viscous force on walls

$$F_{\tau x} = \int_W \tau_{xj} n_j \mathrm{d}W,$$

where W is the surface on which no-slip condition is defined (top and bottom wall of the channel) and $j = x, y, z$. Spanwise and vertical components are negligible compared to the streamwise. The initial transient behaviour is confined in the first $30h/U_b$ time units of the simulation (see Kopera 2011). Two flow-through times were allowed before the averaging was initiated, in order to be certain that no transient behaviour is present in the domain. The statistics of pressure, velocity and Reynolds stress tensor components were collected.

The time history of the spatially averaged reattachment length was used to check statistical convergence with X_r staying within 0.1% of the final value during the last flow-through time and bounded by $\pm 0.4\%$ limit in the last four flow-through times (see Kopera 2011). This provides a reasonable level of confidence in the convergence of the collected statistics.

3.4.1. *Pressure field*

Fig. 7 shows time and spanwise averaged contours of the pressure coefficient, defined as

$$C_P = \frac{P - P_0}{\frac{1}{2}\rho U_b^2},$$

where P_0 is a reference pressure taken at $x = -4h$, $y = 1.5h$. There is a clear pressure drop zone originating at the step edge and spanning up to approximately $x = 4.2h \approx \frac{1}{2}X_r$.

Figure 8 shows static pressure variations across the channel at four different locations in the outflow channel, the reference pressure P_w taken at the top wall at respective locations. The figure shows that the pressure deficit in the recirculation zone is mainly in

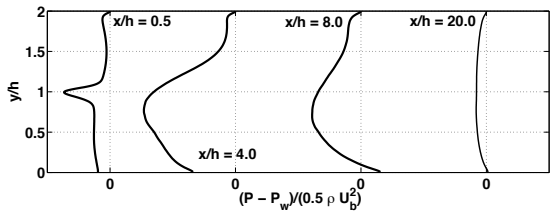

FIGURE 8. Static pressure variation across the channel at four different positions: $x/h = 0.5$, $x/h = 4.0$, $x/h = 8.0$ and $x/h = 20$

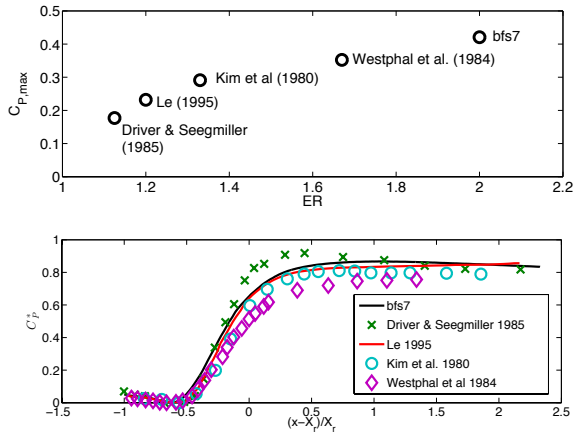

FIGURE 9. Comparison of pressure coefficient with experiments and simulations by Driver & Seegmiller (1985); Kim *et al.* (1980); Westphal *et al.* (1984); Le (1995). (a) Maximum of the static pressure coefficient in different experiments and simulations $C_{P,max}$ against the expansion ratio E_R; (b) Pressure coefficient at the bottom wall using the scaling of Kim *et al.* (1980)

the mixing layer and there is a significant difference in the static pressures at the top and bottom wall throughout the outflow channel. In the recirculation zone ($x/h = 0.5, 4.0$) the difference is in favour of the top wall, while in the reattachment zone ($x/h = 8.0$) the static pressure at the bottom wall is higher. Far downstream in the regeneration zone ($x/h = 20$) the static pressure profile slowly returns towards a uniform distribution across the channel.

Fig. 9(a) plots maximum C_P as a function of the expansion ratio E_R for the present case (bfs7), as well as the previous work (Le 1995; Driver & Seegmiller 1985; Kim *et al.* 1980; Westphal *et al.* 1984). The experimental static pressure maxima in Fig. 9(a) grow with E_R and our new simulations continue this trend. To the author's knowledge there are no simulations and experiments with $E_R > 2$.

In order to investigate the wall pressure distribution further, Fig. 9b presents the bottom wall static pressure coefficient compared with the DNS and experimental datasets. To collapse the results better, the streamwise coordinate was scaled by the reattachment position $x^* = \frac{x - X_r}{X_r}$. Since the reference simulation and experiments were conducted using different expansion ratios, we use a scaling proposed by Kim *et al.* (1980):

$$C_P^* = \frac{C_P - C_{P,min}}{C_{P,BC} - C_{P,min}},$$

where $C_{P,min}$ is the minimum pressure coefficient and $C_{P,BC} = \frac{2}{E_R}\left(1 - \frac{1}{E_R}\right)$ is the

Borda-Carnot pressure coefficient. The DNS simulations (solid lines) collapse particularly well, while the experimental data sets retain some of the E_R dependence.

3.5. *Streamwise velocity field*

Fig. 10a plots the mean streamwise velocity colour-map and streamlines in the recirculation and reattachment with the incoming flow slowly expanding towards the bottom wall, reattaching to it around $x = 8.41h$ then regenerating further downstream into a fully developed channel flow. While in the corner after the step the interaction of the incoming flow, and the fluid trapped by it in the corner after the step allows a recirculation bubble to form. The recirculation bubble turnover time ($T_{BT} \approx 400h/U_b$ integrated along streamlines of the averaged velocity field) is much larger than the flow-through time of the main flow ($T_{FT} \approx 25h/U_b$). Its maximum reverse flow occurs between $x = 2.0h$ and $x = 6.0h$ with $U_{min} = -0.25$ at $x = 3.91$, $y = 0.08$. There is no evidence for a recirculation bubble on the top wall, which is in agreement with earlier work (Le 1995).

In addition to the primary recirculation bubble, streamlines show several additional eddies in the step corner and along the wall (Fig. 10b and c). The vortex at the forward tip of the main secondary eddy has the same anti-clockwise direction as the main secondary eddy. To differentiate between two structures, the main secondary eddy will be called the secondary corner eddy, and the additional structure will be referred to as the secondary eddy extension. The total streamwise dimension of the secondary structures is equal to $1.44h$ (based on the $U = 0$ isoline), although it is difficult to judge the location of the separation point between the two secondary structures, a hint is provided by the position of the $V = 0$ isoline attachment to the bottom wall ($x = 0.99h$). The vertical span of the secondary corner eddy is $0.8h$, which is in excellent agreement with Le *et al.* (1997). The centre of the secondary corner eddy is located at $x = 0.328h$, $y = 0.243h$, and the secondary eddy extension is centred at $x = 1.237h$, $y = 0.025h$.

Closer examination reveals the tertiary corner eddy (Fig. 10c). This resembles the prediction by Moffat (1964) made for the low Reynolds number flow in the vicinity of the sharp corner. The theory predicted an infinite number of eddies decreasing in size and strength in the limit of $Re \to 0$. Computations by Biswas *et al.* (2004) showed two corner eddies for $Re = 1$. Experiments by Hall *et al.* (2003) investigated the secondary vortex in the turbulent backward-facing step flow, however did not reveal any tertiary eddies. In our simulation the tertiary corner eddy size is $0.062h$ in horizontal and $0.11h$ in vertical dimension. Its centre is located at $x = 0.03h$, $y = 0.042h$. This result is in good agreement with Le *et al.* (1997), which report the presence of a tertiary corner eddie of $0.042h$ in size.

Both the secondary eddy extension and the tertiary corner eddies are small structures. In order to resolve them in the simulation, the secondary eddy extension is covered by roughly 5 elements in the streamwise direction and over 1 element in the vertical direction, while the tertiary corner eddy is covered by just over 1 element in the horizontal and 2 elements the vertical direction. Recall that a variable in each element is expanded using 11×11 nodal points, which gives the resolution of roughly 55×11 for the secondary eddy extension and 11×22 for the tertiary corner eddy, showing that both structures are well resolved and there is no evidence of any further corner eddies.

Consistent with these findings are PIV measurements by Hall *et al.* (2003), which indicate that an additional secondary structure might be present in the BFS flow. Their results show that at the tip of the secondary eddy a part of the primary recirculating flow turns just ahead of the secondary vortex and flows in the direction perpendicular to the cross-sectional plane. The authors argued that it is unlikely to be a result of PIV error

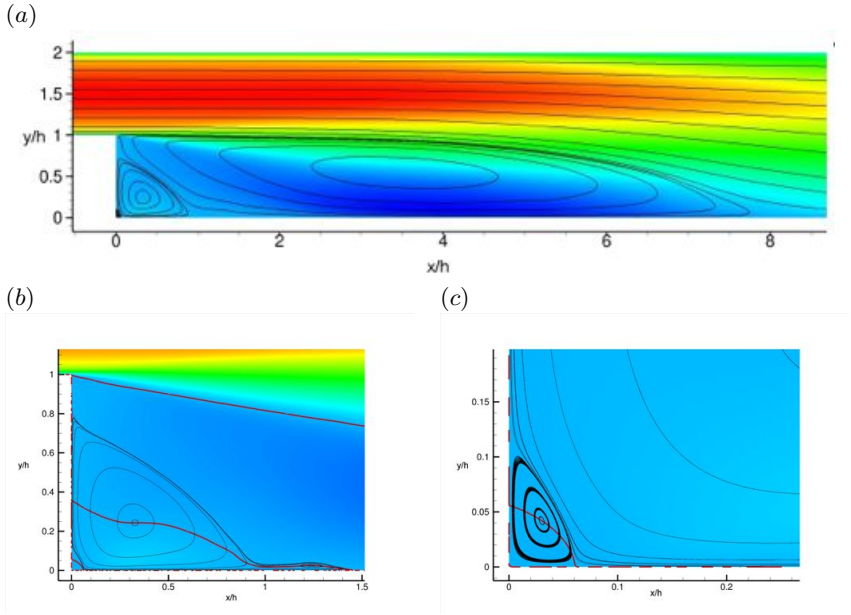

FIGURE 10. U velocity field (colormap) and streamlines (black solid lines). The red solid line marks the $U = 0$ isoline. (a) The recirculation area. (b) Secondary recirculation bubble with an additional structure between $x/h = 1.0$ and $x/h = 1.5$. (c) Tertiary corner bubble.

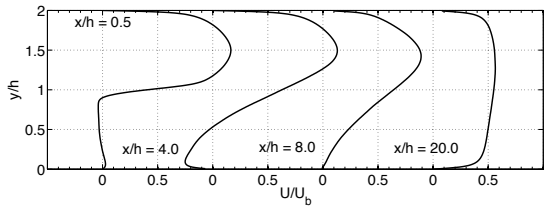

FIGURE 11. U velocity profiles at four different positions: $x/h = 0.5$, $x/h = 4.0$, $x/h = 8.0$ and $x/h = 20$

and concluded, that this might indeed be a new flow structure. This structure coincides in space with the additional secondary vortex revealed by the present study.

It is worthwhile to examine the differences between structures in Fig. 10b and Hall *et al.* (2003). The experimental study revealed a spiral shape of the streamlines in the secondary vortex, which indicates a mass flow into the core that produces a spanwise flow in the secondary vortex. The presence of walls in the experimental setup might cause the secondary vortex to generate Ekman pumping, which would explain the spanwise flow. Additionally, the flow in the spanwise direction in the additional secondary structure could be due to Ekman pumping balancing the flow within the secondary corner eddy, which cannot exist in the present study where streamlines are closed loops or spiral very slowly. Despite differences in streamlines shape, perhaps due the different spanwise boundary conditions, the fact that both structures occur at the same place indicates that the tip of the secondary vortex may indeed contain a further structure in the backward-facing step flow, as suggested by Hall *et al.* (2003).

Fig. 11 shows U profiles at different x locations. Initially the fully developed turbulent flow expands freely into the expanded channel ($x/h = 0.5$) followed by the reversed flow,

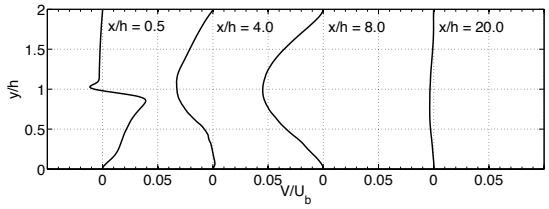

FIGURE 12. V velocity profiles at four different positions: $x/h = 0.5$, $x/h = 4.0$, $x/h = 8.0$ and $x/h = 20$

which is clearly visible at $x/h = 4.0$, but not visible at $x = 8.0h$ profile despite the wall shear stress (Fig 4b) and Table 1 indicating that the mean reattachment position is at $X_r = 8.62$. As the profiles move further downstream they slowly return to those for equilibrium channel flow. Even at $x/h = 20$ the fully developed turbulent channel flow profile has not been reached (see Kopera 2011), in agreement with Le *et al.* (1997). The authors referenced in (Le 1995, p. 118) also report that even at long distances downstream ($50h$ - Bradshaw & Wong (1972)) the velocity profile is still not fully recovered.

3.6. *Spanwise velocity profiiles*

Figure 12 plots profiles of the velocity V. Shortly downstream of the step ($x/h = 0.5$ profile) there is a a strong V gradient in the mixing zone. In the main flow area between $x/h = 4.0$ and $x/h = 8.0$ there is a clear downward movement (negative V). The downward tendency, although minimal, is still present as far as $x = 20h$ downstream of the step, while the recirculation zone close to the step edge exhibits strong upward motion ($x/h = 0.5$). The maximum value of the average vertical velocity $V_{max} = 0.045U_b$ is located at $x = 1.83h$, $y = 0.61h$ and the strongest downwards motion $V_{min} = -0.06U_b$ occurs at $x = 6.58h$, $y = 1.01h$.

3.7. *Persistent streamwise vortices*

Figures 13 and 14 show time-averaged $z-y$ spanwise structures of V, the vertical velocity, and λ_2, the criteria introduced by Jeong & Hussain (1995), for $Re = 9000$ calculations using $L_z = 2\pi$, $L_z = 0.75\pi$ and $L_z = 1.5\pi$. The slices are all at $x = 6.0h$, a bit before the oscillating reattachment line and within the secondary recirculation eddy. λ_2 is the middle eigenvalue of the following symmetric matrix:

$$\mathbf{S^2} + \mathbf{\Omega^2} \tag{3.2}$$

where $\mathbf{S}$ and $\mathbf{\Omega}$ are the symmetric and anti-symmetric components of the velocity stress tensor. λ_2 is useful because it identifies the low pressure zones typically associated with strong vortices and the values of λ_2 plotted are obtained by interpolating the spectral element data onto an evenly spaced mesh, plus some additional local averaging between neighboring points.

For all three domains, spanwise periodic streamwise structures appear. By comparing the time-averaged upwards and downwards motion of the vertical velocity indicated in figure 13a with the zones of time-averaged positive and negative vorticity in 13b, roughly three-four clusters can be identified for the $L_z = 2\pi$ case. These can be related to the three (or four) lobes in the shear stress in the outflow from the recirculation zone in figure 15 and the wavy profile of the mean reattachment line in that figure. These structures cannot be clearly seen when individual times are plotted which raises these questions: Is the observed spanwise periodicity a physical phenomena, or is it an artifact of the imposed spanwise periodicity and the time-averaging?

(*a*)

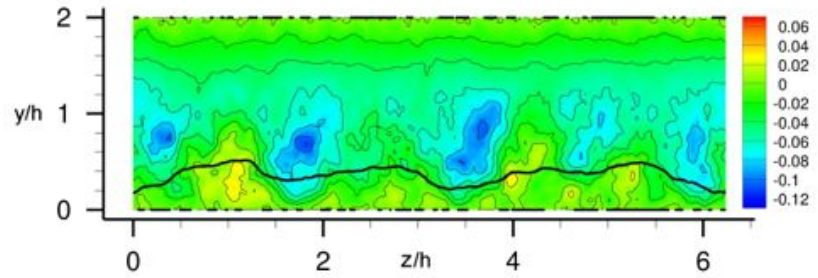

(*b*)

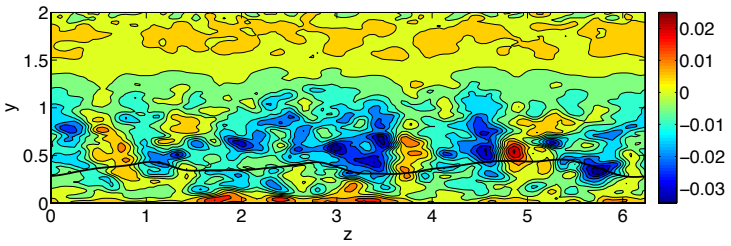

FIGURE 13. Spanwise structure of the time-averaged vertical velocity V in (a) and vorticity criteria λ_2 (3.2) in (b) at $x = 6h$ for the $L_z = 2\pi h$ $Re = 9000$ calculation. Four subsiding (blue) structures can be identified in V across the $y/h = 0.6$ line at z/h=1.6, 3.6, 4.8 (weakly) and crossing the periodic boundary at $z/h = 0 = 2\pi$. The upwelling (yellow) zones are less distinct, but four zones between the subsiding structures can be identified at z/h =1, 2.6, 4 and 5.3. In λ_2, there are blue (left)-yellow (right) pairs across $y/h = 0.6$ about z/h=3.6 and 4.8 and less distinct pairs across $y/h = 0.3$ at $z/h = 1$ and 6.

(*a*) (*b*)

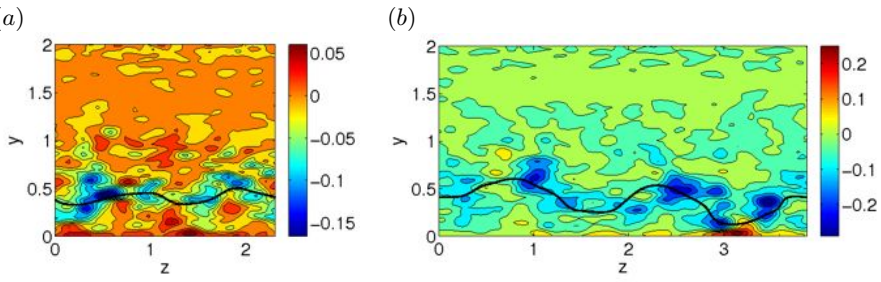

FIGURE 14. Spanwise structure of the time-averaged vorticity criteria λ_2 (3.2) for at $x = 6.0h$: a) The $L_z = 0.75\pi$ simulation. b) The $L_z = 1.25\pi$ simulation. Bold solid line marks $U = 0$. Two streamwise vortices can be identified for each, but only for b), $L_z = 1.25\pi$, is the spacing roughly the same as for the $L_z = 2\pi h$ calculation.

The purpose of the additional $L_z = 0.75\pi$ and $L_z = 1.25\pi$ calculations is to determine how the periodicity of the structures depends on the periodicity of the domain. To reduce the computational expense, their initial conditions were generated from the primary $L_z = 2\pi$, $N_z = 128$ simulation by keeping only the first 24 and 40 Fourier modes respectively, that is $N_z = 48$ and $N_z = 80$, and adding some random noise, then running for $T = 120h/U_b$ time units. Structures can be inferred by comparing the variations in the $U = 0$ line, which indicate recirculation lobes, with the λ_2 criterion. Using this comparison, figure 14a has two structures over a much shorter spanwise spacing that

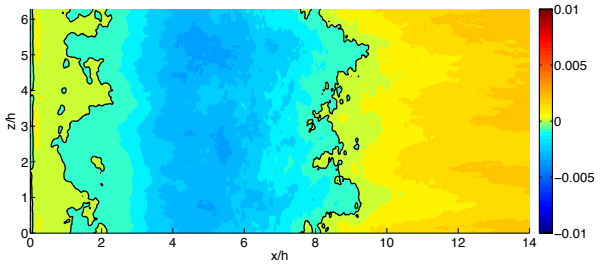

FIGURE 15. Average shear stress at the bottom wall. Solid black line marks $\tau_w = 0$ and separates the regions of forward and reversed flow. There are roughly three lobes on the reattachment line near $x/h = 8.5$ at z/h =1, 2.6 and 5.2 that could be associated with the blue-yellow λ_2 pairs at z/h =1, 3.6 and 4.8 in figure 13b.

was used by the figure 13 calculations. In contrast, even though figure 14b also has two dominant structures, this is with nearly twice the spanwise domain of 14a and roughly the same spanwise spacing of the structures as in figure 13. This allows us to conclude that the spacings in figure 13 for the primary $L_z = 2\pi$ case are physical.

To support our conclusion that the spanwise structures are persistent and not an artifact of the local time-averaging, we have looked at the spanwise spectra and determined how the time-averaging suppresses peaks. The time averaging used suppresses the typical peaks in V at individual times by roughly a factor of 6 and we estimate that it would require averages over significantly longer periods than those used in the present work in order for the persistent structures to disappear. The spectral evidence for the persistence of the structures is a broad plateau for $k_z \leq 3$ with a turbulent-like power-law decay for $k_z > 3$ in in the E_{vv} spectrum in figure 6. The average over all y of the E_{vv} spectra at $x = 4h$ has a similar plateau, which indicates that large excursions in V at $x = 4h$, potentially similar to those for U and W, have been suppressed by the streamwise vortical structures. Together, the contour plots in figures 13-14, plus the V spectrum in figure 6d, support a view that the time-averaging is acting like a coarse-grained filter that removes the small-scale turbulent fluctuations, thereby allowing us to see the persistent large-scale structures.

We note that in the stability analysis of Barkley *et al.* (2002), the leading instability modes took the form of steady elongated three-dimensional rolls that were largely confined to the separation bubble attached to the step, and that these general features appear similar to the quasi-steady structures we have observed here. Barkley *et al.* (2002) suggest that the underlying mechanism for the steady instability mode is centrifugal, but confined within the separation bubble and so not of Taylor–Görtler type. However, the spanwise wavelengths are here of order two step heights, compared to an onset wavelength of order seven step heights in the steady laminar flow (Barkley *et al.* 2002, figure 8). Without further analysis, it is difficult to be categorical about the linkage between the two studies, or physical mechanism in the present case.

3.8. *Average wall shear stress*

Fig. 15 shows the average wall shear stress at the bottom wall. The three to four spanwise variations of the $x \approx 8$ main reattachment line come from the spanwise lobes discussed in Sec. 3.7. The structure of the secondary corner eddy can also be observed. The line at $x \approx 2$ is the leading edge of the secondary eddy extension. It corresponds to the structure of the primary reattachment line. The tertiary corner eddy is visible as well at $x \approx 0.1$,

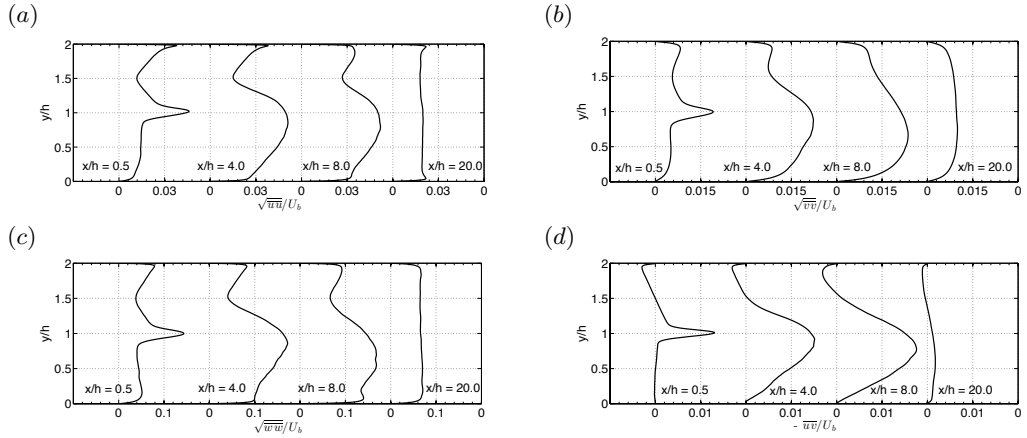

FIGURE 16. Turbulence intensity profiles $\sqrt{\overline{u'u'}}/U_b$, $\sqrt{\overline{v'v'}}/U_b$, $\sqrt{\overline{w'w'}}/U_b$ and Reynolds stress profiles $\sqrt{\overline{u'v'}}/U_b$

but does not span the entire width of the domain, as two regions of positive flow near the step wall are present at $y = 1.8$ and $y = 3.9$.

3.9. *Turbulence intensity and Reynolds shear stress*

Figure 16 plots the streamwise evolution of profiles of turbulence intensities $\sqrt{\overline{u'u'}}$, $\sqrt{\overline{v'v'}}$, $\sqrt{\overline{w'w'}}$ and Reynolds shear stress $\overline{u'v'}$ normalised with U_b^2. Turbulence intensity profiles (Fig. 16a-c) show a sharp increase in the mixing layer at $x = 0.5h$ downstream from the step with the streamwise turbulence intensity component maintaining its original peak near the top wall until $x = 8.0$ when the flow enters the reattachment zone. Further downstream the peak slowly regenerates. The spike in the mixing layer at $x = 0.5h$ widens gradually to $y < 1h$ as $x = 4.0h$ and $x = 8.0h$.

The first appearance of a near-wall peak in $\overline{u'u'}$ for the bottom wall is around $x = 8.0h$ in the reattachment area and grows as the flow moves downstream, although the initial profile from the inlet channel is never fully recovered within the domain. The peak value $(\overline{u'u'})_{max} = 0.054U_b^2$ is located at $x = 5.3h$, $y = 0.85h$.

The vertical turbulence intensity component evolves similarly to the streamwise component in the mixing layer. The maximum $(\overline{v'v'})_{max} = 0.026U_b^2$ is located at $x = 5.63h$, $y = 0.74h$. As the flows undergoes reattachment, the slight initial peak at the wall disappears and does not regenerate further downstream, on either the top or the bottom wall. The $\overline{v'v'}$ profile takes a more convex shape than the initial profile further downstream. This is due to the increased turbulence intensity in the middle of the channel.

The spanwise component $\overline{w'w'}$ follows the behaviour of the other turbulence intensity components in the mixing layer with its maximum $(\overline{w'w'})_{max} = 0.035U_b^2$ located at $x = 6.27h$, $y = 0.75h$, and increased turbulence intensity in the regeneration zone found in the middle of the channel when compared with the inlet profile.

The Reynolds shear stress component reaches its maximum $(-\overline{u'v'})_{max} = 0.019$ at $x = 5.47h$, $y = 0.8h$ and its initial profile is nearly recovered by $x = 20.0h$. The middle part of the profile is still not linear.

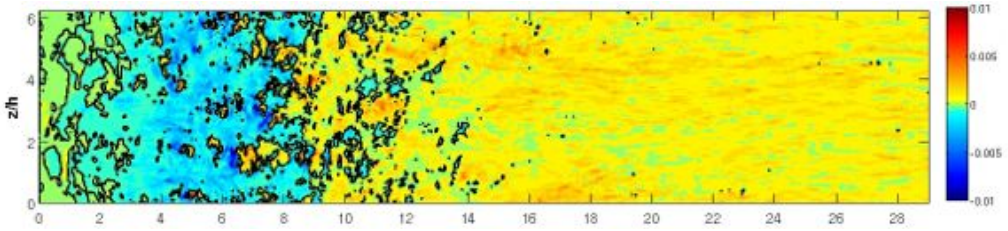

FIGURE 17. Instantaneous streamwise component of the wall shear stress (wall traction) at the bottom wall. Solid black lines marks $\tau_w = 0$ and separate the regions of forward (warm colors) and reversed (cold colors) flow

3.10. *Instantaneous results and dynamics of BFS flow*

This section focuses on instantaneous results with special attention to the dynamics of the reattachment position. First, wall shear stress dynamical behaviour is analysed, followed by the interactions of vortical structures with the recirculation bubble.

3.10.1. *Wall shear stress*

Fig. 17 plots an instantaneous contour of the streamwise component of the wall shear stress (we refer only the streamwise component each time we discuss wall shear stress), and for reference, compare positions with averaged wall shear stress in Fig. 15 and a mean reattachment position at $X_r = 8.62h$. Unlike those average profiles and position, Fig. 17 does not have a well-defined reattachment position, but instead a complex structure of forward and reverse flow patches. Four main regimes can be defined: forward flow for $x > 12h$, mixed flow - the reattachment zone for $6 < x < 12$, reversed flow for $2.5 < x < 6$ and the secondary bubble with forward flow near the wall for $x < 2.5$. Very close to the wall is in addition the tertiary bubble exists, as discussed in section 3.5, however this is not clearly visible in Fig. 17.

Fig. 17 shows a footprint of streamwise vortices discussed in Section 3.7. Three long streamwise areas of positive flow are forming between $x/h = 6.0$ and $x/h = 9.0$. On a sequence of images in (Kopera 2011, pg. 116) and an on-line movie it can be seen that at the same time the reverse flow area is moving downstream, which results in an increase of the instantaneous reattachment length X_r. At $t = 65.0h/U_b$ the three streaks of forward flow start to merge together into a larger spanwise structure that starts to cut-off a zone of reverse flow between $x = 7.5h$ and $x = 9.0h$. This enclosed reverse flow zone moves downstream and disappears at around $t = 70.0h/U_b$.

At the same time the complex structure of the secondary bubble can be observed. Instead of one compact zone of positive flow there is an intricate mixture of forward and reverse flow patches. No clear correlation between the behaviour of the main reattachment location and secondary bubble is visible.

3.10.2. *Oscillations of the reattachment position*

Fig. 18 plots the spanwise averaged time evolution of the bottom wall shear stress with the solid line denoting zero shear stress and the grey area indicating the reverse flow zone. The temporal variations in the reattachment length form an oscillating pattern with a leaning saw-tooths. The reattachment length increases slowly in a roughly linear fashion with an average slope of $0.3U_b$, then decreases more rapidly until an area of forward flow forms upstream of the main reattachment position, for example for $t = 65 - 67.5h/U_b$. This forward flow zone eventually overtakes the downstream reverse flow zone, thus closing the leaning saw-tooth shape, as at $t = 70h/U_b$. Simultaneously the upstream limit

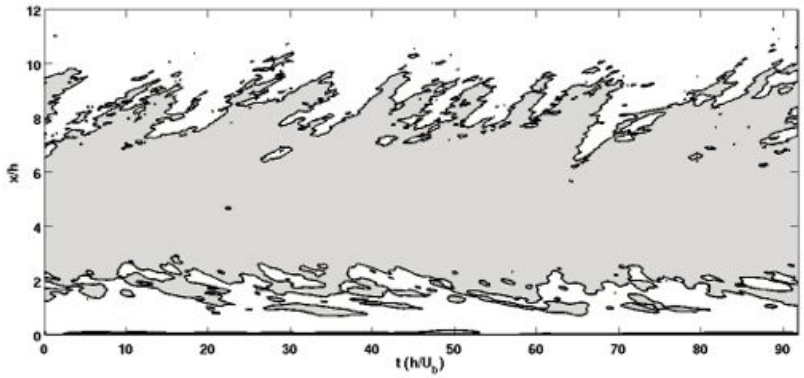

FIGURE 18. Space-time plot of spanwise-averaged contours of the instantaneous streamwise component of the shear stress at the bottom wall. Solid black line marks $\tau_w = 0$ and separates the regions of forward (white) and reversed (grey) flow.

of the new forward flow area becomes the new reattachment position. This oscillating pattern is not very regular and carries small scale structures on top of it.

The secondary bubble lacks the small scale structure of the main recirculation zone, yet exhibits a similar inverse pattern. Its pattern is not as clear as the primary one, with a negative slope to the secondary structures of roughly $-0.08U_b$. Similar behavior on the tertiary corner bubble has not been observed.

Similar oscillatory behavior of the main reattachment position in a turbulent flow was observed by Le *et al.* (1997); Schafer *et al.* (2009). Le *et al.* (1997) reports a saw-tooth shape to the X_r - t plot for $Re_h = 4250$ (originally $Re = 5100$ based on U_0) and $E_R = 1.2$. Compared to the current simulation, doubling Reynolds number results in a doubling of the speed of the reattachment length, which could also be influenced by the differences in geometry (expansion in a channel flow vs boundary layer flow over a step). Another similarity between the two cases is the frequency of the oscillations. In both figures there are approximately 8 saw-tooth shapes in $100h/U_b$ period.

Following Schafer *et al.* (2009), we would like to explain the oscillations of the reattachment position by a visual inspection. However, this is too difficult due to the complexity of our vortical structures compared to those in the transitional flow (Schafer *et al.* 2009), so instead we use the spanwise averages of the pressure fluctuations in Fig. 19, where the black solid lines mark the $U = 0$ isolines and the colormaps show the pressure fluctuations. Initially the recirculation area forms a compact bubble ($tU_b/h = 62.5$) with the low pressure zone (dark blue) inducing the bubble to stretch downstream at $tU_b/h = 64$. At $t = 65.0h/U_b$, the bubble then starts to separate and the separated part of the reversed flow travels downstream with the low pressure zone, while the main recirculation bubble contracts quickly ($tU_b/h = 66$).

Fig. 19 also shows that the mechanism governing the flapping of the primary reattachment position in turbulent flow is the same as for the transitional case studied by Schafer *et al.* (2009). The vortical structures that grow in the mixing layer interact with the wall by inducing a zone of reversed flow near the wall, which causes the recirculation bubble to stretch. As the structure is convected downstream it carries the reversed flow zone with it, which then causes the recirculation bubble to split. As the reversed flow zone disappears, the reattachment length rapidly shrinks. The difference for turbulent flow is that the vortical structures in the mixing layer are more complex than those in a transitional flow.

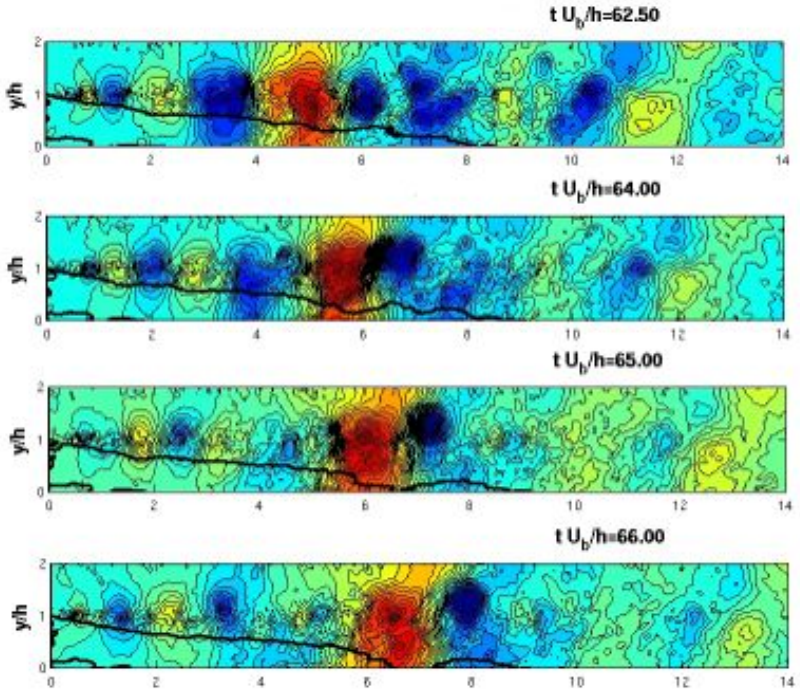

FIGURE 19. Spanwise averaged contours of instantaneous pressure fluctuations at four different times. Solid black line marks $U = 0$ and separates the regions of positive and negative flow. The time sequence visualizes the interaction of low pressure regions with the recirculation bubble, marked by a solid black line.

3.10.3. *Frequency spectra*

The quantitative analysis of the oscillatory behaviour of the reattachment position can be performed by studying the frequency spectra of pressure and streamwise velocity fluctuations near the reattachment position. Fig. 20 shows the power spectra of both u' (plots (a)) and p' (plots (b)) for different locations in the flow. The positions of the measurements points are depicted on the top right plot. Here we report data from selected measurement points, the full set is available in Kopera (2011).

Point #1 is located in the inlet channel. The spectrum shows clearly the peak corresponding to the inlet periodicity generated by the regeneration technique ($St = 0.127$), and subsequent subharmonics. The following plots will examine whether this frequency is present elsewhere in the flow and whether it influences the oscillations of the reattachment position.

Spectra near the step edge (point #2) show only a slight peak at the regeneration frequency $St = 0.127$, both for the velocity and pressure fluctuations. The same frequency shows up in the velocity fluctuations at point #4 in the main flow region, but is less visible in the mixing layer at point #5 with the spike at $St = 0.117$. The regeneration frequency is not, however, pronounced at point #9 in the reattachment region, as it shows up only as a minor spike in the pressure fluctuations spectrum. This indicates that even though the regeneration frequency is present in the flow, it has no dominant influence on the vortex formation in the mixing layer.

At the reattachment point #9 the most dominant frequency in both velocity and pressure fluctuation spectra is $St = 0.078$, which also shows up at the step edge (#2),

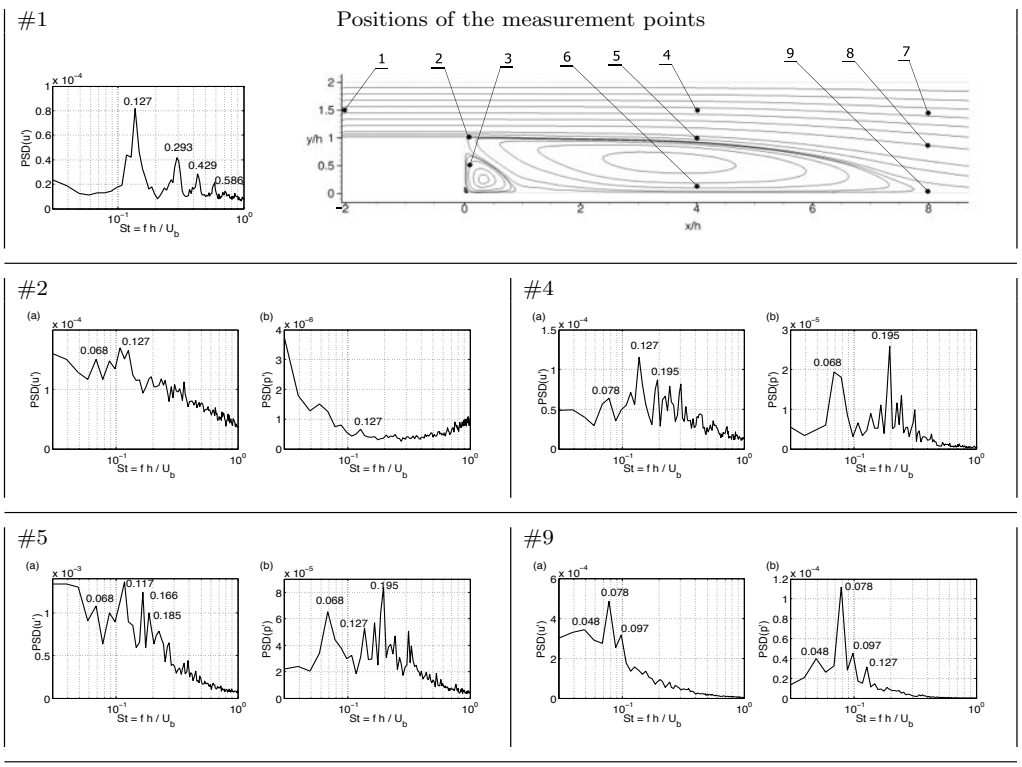

FIGURE 20. Spanwise averaged power spectrum density for velocity fluctuation u' (a) and pressure fluctuation p' (b) at different location in the flow field. Positions of the measurement points are depicted in the top right plot. Point coordinates: #1 (x=$-2h$, y=$1.5h$), #2 (x=$0.1h$, y=h), #4 (x=$4h$, y=$1.5h$), #5 (x=$4h$, y=h), #9 (x=$8h$, y=$0.01h$). Complete data for all measurement points is available in Kopera (2011)

in the mixing (#5)and the main flow (#4) zones (often as $St = 0.068$), but there is no evidence of it at the inlet channel (#1). This clearly indicates that the presence of a vortex (represented by a pressure fluctuation) and behavior of the reattachment position is correlated and tuned to a characteristic frequency of $St \approx 0.068 - 0.078$. This result agrees with previous findings of Le *et al.* (1997) who report $St \approx 0.06$ as a frequency of the reattachment flapping. Similarly Silveira Neto *et al.* (1993) provides the value $St = 0.08$ for large Kelvin-Helmholtz structures in the mixing layer. Schafer *et al.* (2009) report $St = 0.266$, however the quantitative agreement in this case cannot be expected due to the presence of the laminar flow at the inflow of this simulation.

At point #5 in the mixing layer and #4 in the main flow the higher frequency of $St = 0.195$ shows up, which is not present in the reattachment region (#9) or the inflow channel (#1). Its origins cannot therefore be explained by the regeneration technique or the reattachment flapping.

In order to further exclude the influence of the regeneration frequency on the reattachment oscillations, an additional simulation with shorter regeneration length ($L_i = 5h$) was performed. The spanwise length was set to $L_z = 0.75\pi$ and the spanwise resolution $N_z = 48$. Figure 21 presents the spectra taken in the inlet channel (point #1) and reattachment zone (point #9) of this additional simulation. It clearly shows the new regeneration frequency of $St = 0.219$ and its harmonics in the inflow. The characteristic frequency

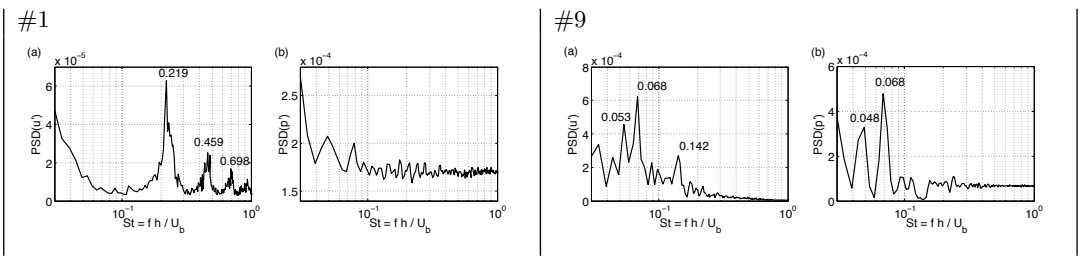

FIGURE 21. Spanwise averaged power spectra of streamwise velocity fluctuation u' (a) and pressure fluctuation p' (b) for two points of the the additional simulation. The points coordinates are defined in Fig. 20

in the reattachment zone is $St = 0.068$, which is in the regime $St = 0.068 - 0.078$ identified as a characteristic frequency of the recirculation zone. This shows that the increased regeneration frequency does not have an influence on the reattachment oscillations.

4. Conclusions

Direct numerical simulations of turbulent flow over a backward-facing step were performed for Reynolds numbers up to $Re_h = 9000$, with enough spatial and temporal resolution to allow the first numerical investigation of the interaction of the streamwise and spanwise vortices with the reattachment position. Finding that both of the average position of the reattachment of the recirculation eddy and its frequency are consistent with experiments.

A crucial part in achieving this was providing a turbulent flow into the domain using a modification of the technique of Lund *et al.* (1998). To accomplish this, the inflow channel was extended, within which a periodic turbulent channel flow was created and maintained using a copy boundary condition. The resulting turbulent flow was then fed into the main part of the backward facing step calculation. To keep the mass flow constant, Greens function corrections were applied to the periodic flow, yielding accurate flow rate control with little extra computational expense. With this turbulent inflow, the calculations were able to reproduce the streamwise velocity profiles and turbulence intensity profiles of Kim *et al.* (1987) and Moser *et al.* (1999).

The following properties agree with experiments and previous computations, validating this approach: The mean reattachment length $X_r = 8.62h$ for $E_R = 2.0$ and $Re_h = 9000$ and for the $Re_h = 6000$ preliminary simulation $X_r = 8.16h$, both of which match the values from Armaly *et al.* (1983) for a two-dimensional turbulent flow over a BFS with $E_R = 2.0$. Furthermore, taking into account the differences in Re_h and E_R and scaling the abscissas by X_r, the streamwise profile of the coefficient of friction at the bottom wall agree with previous experimental and computational results, as does the position of the maximum negative skin friction at $0.62X_r$ and the dependence of the value of maximum negative peak on Re_h (Adams & Johnston 1988; Jovic & Driver 1995; Le *et al.* 1997; Spazzini *et al.* 2001, see fig. 4 and tab. 1). For pressure statistics, the coefficient of pressure at the bottom wall obeys the scaling of Kim *et al.* (1980) and the position of maximum C_P with respect to X_r, confirming the strong dependence upon E_R found in previous work for lower expansion ratios (Driver & Seegmiller 1985; Kim *et al.* 1980; Westphal *et al.* 1984; Le 1995, see fig. 9).

What these calculations show that previous calculations did not is that addition to

the main recirculation bubble, the time and spanwise averaged velocity field provides evidence for the secondary and tertiary corner eddies with this additional feature: Paired with the secondary eddy, an additional vortical structure appears that is located at its downstream tip and rotating in the same direction. Weak evidence for such a structure has appeared in experiments (Hall *et al.* 2003), but the PIV measurements were not conclusive. Besides confirming the experimental observation, figure 13 identifies some of the spanwise structure within the secondary eddy using time averages of the velocity field V and vorticity criteria λ_2 (3.2). Three to four clusters of positive and negative pairs are noted, along with a similar structure appearing as lobes along the reattachment line in figure 15. Figure 14 indicates that the spacing of these lobes is physical based on the changes in spacing between the lower L_z calculations.

Perhaps the most complex dynamics identified by these simulations are the coherent oscillations and other quasi-periodic behaviour associated with reattachment. This includes oscillations in the reattachment position, a saw-tooth shape for the wall shear stress associated with this reattachment and reattachment flapping. Comparisons between the frequencies reported here and experimental frequencies are in qualitative agreement, with the turbulent inflow being crucial in achieving this agreement as similar agreement was not found for simulations with laminar inflows (Schafer *et al.* 2009). This shows that when attempting to reproduce experimental results, one needs to do more than just match the domain, essential boundaries and Reynolds numbers. The nature of the external forcing or inflow must also be taken into account.

REFERENCES

Abbot, D.E. & Kline, S.J. 1962 Experimental investigations of subsonic turbulent flow over single and double backward-facing steps. *Transactions of the ASME. Series D, Journal of Basic Engineering* **84** (-1).

Adams, E.W. & Johnston, J.P. 1988 Effects of the separating shear layer on the reattachment flow structure. part 1: Pressure and turbulence quantities. part 2: Reattachment length and wall shear stress. *Experiments in Fluids* **6**, 400–408,493–499.

Armaly, B.F., Durst, F., Pereira, J.C.F. & Schonung, B. 1983 Experimental and theoretical investigation of backward-facing step flow. *Journal of Fluid Mechanics Digital Archive* **127** (-1), 473–496.

Barkley, Dwight, Gomes, M Gabriela M & Henderson, Ronald D 2002 Three-dimensional instability in flow over a backward-facing step. *Journal of Fluid Mechanics* **473**, 167–190.

Biswas, G., Breuer, M. & Durst, F. 2004 Backward-facing step flows for various expansion ratios at low and moderate Reynolds numbers. *Transactions of the ASME* **126** (-1), 362 – 374.

Blackburn, H.M. & Sherwin, S.J. 2004 Formulation of a galerkin spectral element fourier method for three-dimensional incompressible flows in cylindrical geometries. *Journal of Computational Physics* **197**, 759–778.

Bradshaw, P. & Wong, F.Y.F. 1972 The reattachment and relaxation of a turbulent shear layer. *Journal of Fluid Mechanics Digital Archive* **52** (01), 113–135.

Cantwell, C.D. 2009 Transient growth of separated flows. PhD thesis, University of Warwick.

Chandrsuda, C. & Bradshaw, P. 1981 Turbulence structure of a reattaching mixing layer. *Journal of Fluid Mechanics* **110**, 171–194.

Driver, D.M. & Seegmiller, H.L. 1985 Features of a reattaching shear layer in divergent channel flow. *AIAA Journal* **23** (2), 163–171.

Durst, F. & Tropea, C. 1981 Turbulent, backward-facing step flows in two-dimensional ducts and channels. In *Proceedings of the Fifth International Symposioum on Turbulent Shear Flows*, pp. 18.1–18.5. Cornell University.

Friedrich, R. & Arnal, M. 1990 Analysing turbulent backward-facing step flow with the

lowpass-filtered Navier-Stokes equations. *Journal of Wind Engineering and Industrial Aerodynamics* **35**, 101–228.

Hall, S.D., Behnia, M., Fletcher, C.A.J. & Morrison, G.L. 2003 Investigation of the secondary corner vortex in a benchmark turbulent backward-facing step using cross-correlation particle imaging velocimetry. *Experiments in Fluids* **35**, 139–151.

Jeong, J. & Hussain, F. 1995 On the identification of a vortex. *Journal of Fluid Mechanics* **285**, 69–94.

Jovic, S. & Driver, D. 1994 Backward-facing step measurements at low Reynolds number. *NASA Tech. Mem.* p. 108807.

Jovic, S. & Driver, D. 1995 Reynolds number effect on the skin friction in separated flows behind a backward-facing step. *Experiments in Fluids* **18**, 464–467.

Kaikstis, L., Karniadakis, G. E. & Orszag, S. A. 1991 Onset of three-dimensionality, equilibria, and early transition in flow over a backward-facing step. *Journal of Fluid Mechanics* **231**, 501–538.

Karniadakis, G.E., Israeli, M. & Orszag, S.A. 1991 High-order splitting methods for the incompressible Navier-Stokes equations. *Journal of Computational Physics* **97**, 414–443.

Karniadakis, G.E. & Sherwin, S.J. 2005 *Spectral/hp element methods for computational fluid dynamics*. Oxford University Press.

Kim, J., Kline, S.J. & Johnston, J.P. 1980 Investigation of a reattaching turbulent shear layer: Flow over a backward-facing step. *Transactions of the ASME. Journal of Fluid Engineering* **102** (-1), 302–308.

Kim, J., Moin, P. & Moser, R. 1987 Turbulent statistics in fully developed channel flow at low Reynolds number. *Journal of Fluid Mechanics* **177** (-1), 133–166.

Kopera, M.A. 2011 Direct numerical simulation of turbulent flow over a backward-facing step. PhD thesis, University of Warwick.

Le, H. 1995 Direct numerical simulation of turbulent flow over a backward-facing step. PhD thesis, Stanford University.

Le, H, Moin, P. & Kim, J. 1997 Direct numerical simulation of turbulent flow over a backward-facing step. *Journal of Fluid Mechanics* **330** (-1), 349–374.

Lund, T. S, Wu, X H & Squires, K D 1998 Generation of turbulent inflow data for spatially-developing boundary layer simulations. *Journal of Computational Physics* **140** (2), 233–258.

Moffat, H.K. 1964 Viscous and resistive eddies near a sharp corner. *Journal of Fluid Dynamics* **18** (-1), 1–18.

Moser, R., Kim, J. & Mansour, N. 1999 Direct numerical simulation of turbulent channel flow up to $\mathrm{Re}_\tau = 590$. *Physics of Fluids* **11** (4), 943–945.

Orszag, S.A., Israeli, M. & Deville, O. 1986 Boundary conditions for incompressible flows. *Journal of Scientific Computing* **75**.

Schafer, F., Breuer, M. & Durst, F. 2009 The dynamics of the transitional flow over a backward-facing step. *Journal of Fluid Dynamics* **623**, 85–119.

Silveira Neto, A., Grand, D., Metais, O. & Lesieur, M. 1993 A numerical investigation of the coherent vortices in turbulence behind a backward-facing step. *Journal of Fluid Mechanics* **256**, 1–25.

Spazzini, P.G., Iuso, G., Oronato, M., Zurlo, N. & Di Cicca, G.M. 2001 Unsteady behaviour of back-facing step flow. *Experiments in Fluids* **30**, 551–561.

Westphal, R.V., Johnston, J.P. & Eaton, J.K. 1984 Experimental study of flow reattachment in a single-sided sudden expansion. *NASA STI/Recon Technical Report N* **84**, 18571.

Yoshioka, S., Obi, S. & Masuda, S. 2001 Turbulence statistics of periodically perturbed separated flow over backward-facing step. *Journal Heat and Fluid Flow* **22**, 393–401.